Supplemental Material: The Effect of Confinement on Capillary Phase Transition In Granular Aggregates

Siavash Monfared,[1,*] Tingtao Zhou,[1,†] José E. Andrade,[1,‡] Katerina Ioannidou,[2,3,§]
Farhang Radjaï,[2,¶] Franz-Josef Ulm,[4,**] and Roland J.-M. Pellenq[5,3,††]

[1]*Division of Engineering and Applied Science,*
California Institute of Technology, Pasadena, CA 91125, USA.[‡‡]
[2]*CNRS, University of Montpellier, LMGC,*
163 rue Auguste Broussonnet F-34090 Montpellier, France.
[3]*MultiScale Material Science for Energy and Environment UMI 3466*
CNRS-MIT-Aix-Marseille Universitè Joint Laboratory, Cambridge, MA 02139, USA.
[4]*Department of Civil and Environmental Engineering,*
Massachusetts Institute of Technology, Cambridge, MA 02139, USA.
[5]*Department of Physics, Georgetown University, Washington, D.C. 20057, USA.*

(Dated: November 16, 2020)

GENERATION OF DISORDERED POROUS MATERIALS

To explore the role of structural disorder and confinement on capillary pressure fields, pore fluid criticality and liquid-gas phase transition, a number of porous structures are created. More specifically, a single realization of non-overlapping monodisperse spherical particle packings in three-dimensional space (3D) are considered with the intent of creating locally varying confinement through introducing spatial disorder in particle positions. Three structures, A, B and C are created with imposed spatial disorder and a constant packing fraction, $f_s = 0.43$. A fourth structure, D is created with a higher packing fraction ($f_s = 0.5$) and structural disorder similar to C. Structure A - the reference configuration - contains periodic arrangement of N_p monodisperse particles of radius R in a cubic box of size $L_x = L_y = L_z = L$ with periodicity $l = L/\sqrt[3]{N_p}$. For structures B and C, disorder is introduced through random Monte-Carlo moves applied to each particle with an apparent pore radius of $R_{\text{app.}} = \lambda R$ with $\lambda \in [1, l/(2R))$. The λ parameter reflects the degree of spatial disorder of the particles varying from a quasi-ordered state $\lambda = l/(2R)$ to a disordered one $\lambda = 1$ [1]. To this end, three samples are created with $\lambda \in \{1.064, 1.021, 1.0\}$, $N_p = 512$, $L = 80$ nm, $R = 4.7$ nm and overall packing fraction $f_s = 0.43$. This method of generating porous structures has been employed before to study the effective elasticity [2] and the failure of disordered porous media [3]. To explore the effect of packing fraction, structure D is created with $f_s = 0.50$, $N_p = 955$, $L = 80$ nm, $R = 4$ nm, and $\lambda = 1.0$. This is done by utilizing a hybrid Grand Canonical Monte Carlo and Molecular Dynamics (GCMC-MD) method was in LAMMPS [4] In this method, N_p is adjusted to achieve the desired packing fraction while R_{app} is imposed through a short-ranged generalized Lennard-Jones interaction potential, $V(r)$:

$$V(r) = 6\epsilon\left[\left(\frac{\sigma}{r}\right)^{2\gamma} - \left(\frac{\sigma}{r}\right)^{\gamma}\right] \tag{1}$$

with r denoting the inter-particle distance and ϵ representing the well depth between two particles of diameter $\sigma = 2R$. The cut-off radius is chosen to be $r_{\text{cr.}} = 2^{1/\gamma}\sigma$ corresponding to the distance at which the potential $V(r)$ is a minimum and $\gamma = 12$. The apparent particle radius, $R_{\text{app.}}$ is imposed via $\sigma = 2R_{\text{app.}}$. This method of generating porous structures is used for a number of investigations in the literature including the formation of cement hydrates [5–7]. The voronoi tessellation, pair correlation function characterizing spatial disorder and

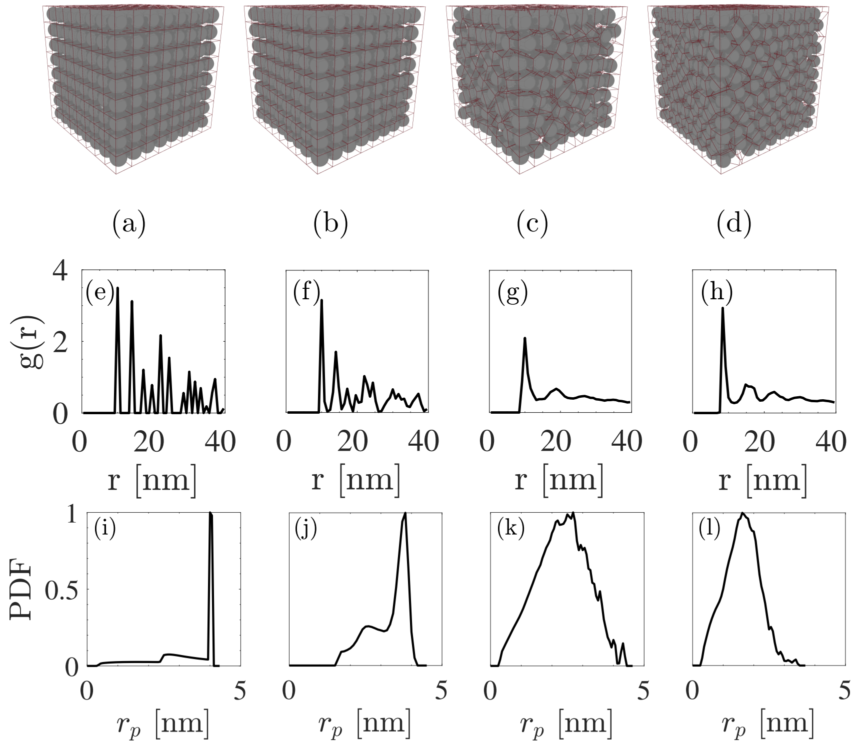

FIG. 1: Voronoi tessellation [8] for structures A (1a), B (1b), C (1c) and D (1d). Radial distribution function of the packing spheres, g(r), for disordered structures A (1e), B (1f), C (1g) and D (1h). The Probability density function for pore radius, r_p computed based on the largest sphere that can fit inside a pore at a given point [9, 10] for structures A (1i), B (1j), C (1k) and D (1l).

the pore size distribution (PSD) for the created granular structures are shown in Fig. 1. As mentioned in the text, the porous structures are created by taking the *negative* of these structures, i.e. *switching* pores and solids.

$N_s^f(r)$ FOR POROUS MATERIALS

As discussed in the text, we characterize the number of interface solid sites in a spherical domain of radius r, $N_s^f(r)$, that influence a given interface fluid site through a connected path in the fluid domain, normalized by the total number of interface solid sites. $N_s^f(r)$ represents the range of fluid-fluid correlations that can develop from the pore surface. Therefore, $N_s^f(r)$ contains information regarding correlation length for the adsorbed fluid or surface-

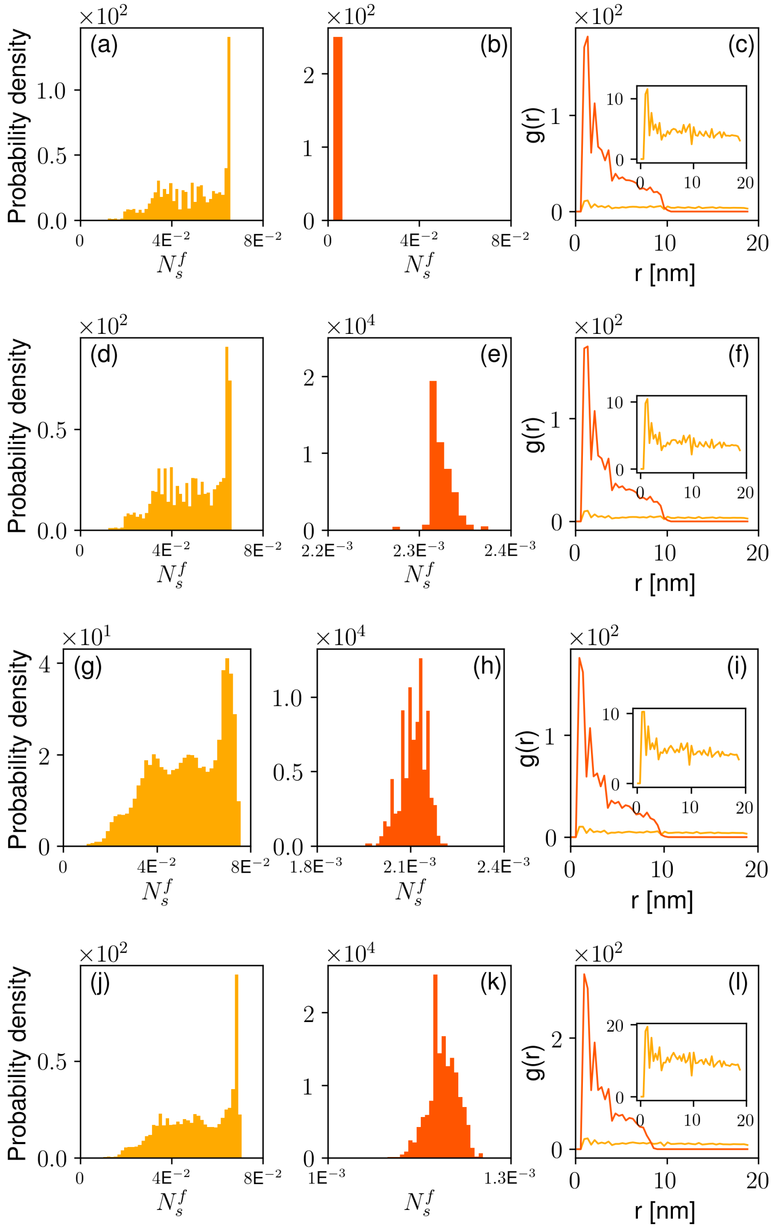

FIG. 2: N_s^f ($r = 20$ nm) for structure $A - D$, GM (2a,2d,2g,2j, respectively) and PS (2b,2e,2h,2k, respectively) along with the partial radial distribution functions for a fluid site at the pore-solid interface with a connected path to a solid site at the pore-solid interface (2c,2f,2i,2l, respectively).

surface correlation length. The distributions of N_s^f ($r = 20$ nm) along with the partial radial distribution functions for fluid sites at the pore-solid interface interacting with solid sites as shown in Fig. 2

CAPILLARY STRESS TENSOR

Generally in density functional theory (DFT) approaches the free energy of the system of particles can be uniquely defined as a functional of inhomogeneous density and for a given Hamiltonian $\mathcal{H}$ and external potential. The equilibrium density distribution ρ_{eq} is obtained through minimization of the free energy functional. The coarse-grained lattice gas model is the discrete version of DFT restricted to nearest neighbor interactions. It provides a mean-field approach to study capillary phenomena. In this study, a liquid-gas fluid mixture is considered. The interface between the two fluids is considered to be diffusive (see for e.g. [11]), i.e. non-zero thickness, with physical quantities smoothly varying between the bulk values in each phase [12]. The coarse-grained lattice gas density functional theory [13, 14] is employed to capture this binary fluid mixture. The Hamiltonian for this model reads:

$$\begin{aligned}\mathcal{H} = &-w_{ff}\sum_{i}^{N}\sum_{j}^{N_i^b}\tau_i\eta_i\tau_j\eta_j \\ &-w_{sf}\sum_{i}^{N}\sum_{j}^{N_i^b}[\tau_i\eta_i\left(1-\eta_j\right)+\tau_j\eta_j\left(1-\eta_i\right)]\end{aligned} \tag{2}$$

where $\tau_i = 0, 1$ and $(1-\eta_i) = 0, 1$ denote the fluid and matrix occupancy variables, respectively. Furthermore, N is the total number of nodes and N_i^b represents number of neighboring sites for node i. Additionally, $w_{ff} > 0$ and $w_{sf} > 0$ are energy parameters that quantify the strength of liquid-liquid and solid-liquid interactions. These strength parameters can be imposed via $y = w_{sf}/w_{ff}$ which is the ratio of these interaction parameters. For a given matrix realization $\{\eta_i\}$, the fluid's free-energy functional, Ψ, reads:

$$\begin{aligned}\Psi\left(\{\rho_i\}\right) = &\frac{1}{\beta}\sum_{i}^{N}[\rho_i\ln\rho_i+\left(\eta_i-\rho_i\right)\ln\left(\eta_i-\rho_i\right)] - \\ &w_{ff}\sum_{i}^{N}\sum_{j}^{N_i^b}\rho_i\rho_j - \\ &w_{sf}\sum_{i}^{N}\sum_{j}^{N_i^b}[\rho_i\left(1-\eta_j\right)+\rho_j\left(1-\eta_i\right)]\end{aligned} \tag{3}$$

where $\beta = 1/k_B T$ with k_B and T denoting Boltzmann constant and temperature, respectively. Additionally, ρ_i denotes normalized fluid density at position $\vec{x}_i$:

$$\rho_i \equiv \rho\left(\vec{x}_i\right) = \frac{\rho_f\left(\vec{x}_i\right)}{\rho_f^b} \qquad \rho_i \in [0,1] \tag{4}$$

with ρ_f^b representing the bulk fluid density. Normalized density field $\rho\left(\vec{x}\right)$ serves as the only order-parameter in the model. For a given chemical potential, μ, minimization of the fluid grand potential functional, $\Omega\left(\{\rho_i\}\right) = \Psi\left(\{\rho_i\}\right) - \mu \sum_i^N \rho_i$, provides the equilibrium density distribution in the system. In the continuum limit, the free energy of the lattice model corresponds to the Cahn-Hilliard model [15]. For a cubic crystal or isotropic medium invariant to the symmetry operations of reflection and of rotation, Taylor expansion of specific free energy of a fluid, f, around a homogeneous state, f_0, reads [16]:

$$f\left(\rho, \vec{\nabla}\rho, \vec{\nabla}^2\rho, ...\right) = f_0\left(\rho\right) + \kappa_1 \vec{\nabla}^2\rho + \kappa_2\left(\vec{\nabla}\rho\right)^2 + ... \tag{5}$$

The mean-field approximation of Cahn-Hilliard-like phase field energy functional representing total free energy of fluid, F^f for a volume V of the solution reads:

$$F = \int_V \left(f_0\left(\rho\right) + \kappa_1 \vec{\nabla}^2\rho + \kappa_2\left(\vec{\nabla}\rho\right)^2 + ...\right) dV \tag{6}$$

Expanding the second term in Eq.(6) by applying the divergence theorem leads to:

$$\begin{aligned} F = &\int_V \left(f_0\left(\rho\right) + \left(\frac{-d\kappa_1}{d\rho} + \kappa_2\right)\left(\vec{\nabla}\rho\right)^2 + ...\right) dV + \\ &\int_{\partial V} \left(\kappa_1 \vec{\nabla}\rho \cdot \vec{n}\right) dS \end{aligned} \tag{7}$$

where $\vec{n}$ is the normal to boundary surface, dS. Neglecting terms beyond second-order results in [16]:

$$\begin{aligned} F = &\int_V \left(f_0\left(\rho\right) + \kappa\left(\vec{\nabla}\rho\right)^2\right) dV + \\ &\int_{\partial V} \left(\kappa_1 \vec{\nabla}\rho \cdot \vec{n}\right) dS \end{aligned} \tag{8}$$

where κ is a gradient energy coefficient that quantifies gradient energy cost of creating inhomogeneity in an otherwise homogeneous system and $\kappa = -d\kappa_1/d\rho + \kappa_2$. In general, κ

depends on density, temperature and concentration among other field variables and can be related to the pair-correlation functions. Thus, the grand potential in the continuum limit for a binary fluid reads:

$$\begin{aligned} G = & \int_V \left(f_0\left(\rho\right) - \mu\rho + \frac{1}{2}\kappa \left(\vec{\nabla}\rho\right)^2 \right) dV + \\ & \int_{\partial V} \left(\kappa_1 \vec{\nabla}\rho \cdot \vec{n} \right) dS \end{aligned} \tag{9}$$

Eq.(9) can be parameterized for the lattice gas model which in the continuum limit reads [15]:

$$\begin{aligned} G = & \int_V [k_B T \left(\rho \ln \rho + \left(1-\rho\right) \ln \left(1-\rho\right)\right) - \mu\rho] dV + \\ & \int_V [\frac{w_{ff}c}{4} a_0^2 \left(\vec{\nabla}\rho\right)^2 - \frac{w_{ff}}{2} c\rho^2] dV + \\ & \int_S d\vec{S} \cdot \left(w_{sf}\rho\vec{n} - \frac{w_{ff}c}{4} a_0^2 \rho \vec{\nabla}\rho \right) \end{aligned} \tag{10}$$

where a_0 represents lattice spacing and c the coordination number, $f_0 = k_B T \left(\rho \ln \rho + \left(1-\rho\right) \ln \left(1-\rho\right)\right) - \frac{c}{2} w_{ff}\rho^2$ and gradient energy coefficient $\kappa = \frac{ca_0^2}{2} w_{ff}$. This energy can be minimized by taking the variational of Eq.(10) with the constraint $\delta\rho|_{\partial V} = 0$ which results in [15]:

$$\begin{aligned} \delta G = & \int_V \left(-cw_{ff}\rho - \frac{ca_0^2}{2} w_{ff} \left(\vec{\nabla}^2\rho\right) - \mu \right) + \\ & \int_V \left(k_B T \ln\left(\frac{\rho}{1-\rho}\right)\right) \delta\rho dV + \\ & \frac{ca_0^2}{2} w_{ff} \int_{\partial V} d\vec{S} \cdot \delta\rho\vec{\nabla}\rho \\ & - \frac{ca_0^2}{4} w_{ff} \int_{\partial V} d\vec{S} \cdot \rho\delta\vec{\nabla}\rho \end{aligned} \tag{11}$$

Furthermore, imposing $\delta \frac{\partial\rho}{\partial\vec{n}}|_{\partial V} = 0$ ensures that surface terms vanish. This, the equilibrium can be expressed as:

$$-cw_{ff}\left(\rho + \frac{a_0^2}{2}\vec{\nabla}^2\rho\right) + k_B T \ln\left(\frac{\rho}{1-\rho}\right) - \mu = 0 \tag{12}$$

From thermodynamics, the classical expression for reference pressure, p_0 reads:

$$p_0 = \mu\rho - f_0 \tag{13}$$

To ensure mechanical equilibrium, $\boldsymbol{\sigma} = p_0\mathbf{1}$ needs to satisfy:

$$-\vec{\nabla}\cdot\boldsymbol{\sigma} = -\vec{\nabla}p_0 = -\vec{f}_{ext} \tag{14}$$

Re-writing Eq. (14) with Eq. (13) results in:

$$-\vec{\nabla}\left(\boldsymbol{\sigma} - \mu\rho\mathbf{1}\right) = \vec{\nabla}\cdot\left(f_0\mathbf{1}\right) = \frac{\partial f_0}{\partial\rho}\vec{\nabla}\rho \tag{15}$$

In order to account for higher order term in the free energy, i.e. $f = f\left(\rho, \vec{\nabla}\rho\right)$ modifies Eq. (15) as follows:

$$-\vec{\nabla}\left(\boldsymbol{\sigma} - \mu\rho\mathbf{1}\right) = \frac{\partial f\left(\rho, \vec{\nabla}\rho\right)}{\partial\rho}\vec{\nabla}\rho \tag{16}$$

Specifically, the second-order term in free energy expansion, Eq. (8) reads:

$$F_1 = \int_V f_1 dV = \int_V \frac{1}{2}\kappa\left(\vec{\nabla}\rho\right)^2 dV \tag{17}$$

Similar to Eq. (15), to ensure mechanical equilibrium due to contributions of Eq. (17), one can write:

$$\vec{\nabla}\cdot\boldsymbol{\sigma} = -\frac{\delta F_1}{\delta\rho}\vec{\nabla}\rho = \left(\frac{-\partial f_1}{\partial\rho} + \vec{\nabla}\cdot\frac{\partial f_1}{\partial\vec{\nabla}\rho}\right)\vec{\nabla}\rho = \kappa\vec{\nabla}\rho\vec{\nabla}^2\rho \tag{18}$$

utilizing vector identity $\vec{u}\cdot\vec{\nabla}\vec{u} = \vec{\nabla}\cdot\left(\vec{u}\otimes\vec{u}\right) - \vec{u}\vec{\nabla}\cdot\vec{u}$, R.H.S. of Eq.(18) can be written as:

$$\kappa\vec{\nabla}\rho\vec{\nabla}^2\rho = \kappa\left(\vec{\nabla}\cdot\left(\vec{\nabla}\rho\otimes\vec{\nabla}\rho\right) - \vec{\nabla}\rho\cdot\vec{\nabla}\left(\vec{\nabla}\rho\right)\right) \tag{19}$$

Additionally, since $\vec{u}\times\left(\vec{\nabla}\times\vec{u}\right) = \frac{1}{2}\vec{\nabla}\left(\vec{u}\cdot\vec{u}\right) - \vec{u}\cdot\vec{\nabla}\vec{u}$, Eq.(18) reduces to:

$$\begin{aligned}\kappa\vec{\nabla}\rho\vec{\nabla}^2\rho &= \kappa\left(\vec{\nabla}\cdot\left(\vec{\nabla}\rho\otimes\vec{\nabla}\rho\right) - \vec{\nabla}\rho\cdot\vec{\nabla}\left(\vec{\nabla}\rho\right)\right)\\ &= -\kappa\left(\left(\frac{1}{2}\vec{\nabla}\left(\vec{\nabla}\rho\cdot\vec{\nabla}\rho\right) - \vec{\nabla}\rho\times\left(\vec{\nabla}\times\vec{\nabla}\rho\right)\right)\right)\\ &\quad \kappa\left(\vec{\nabla}\cdot\left(\vec{\nabla}\rho\otimes\vec{\nabla}\rho\right)\right)\end{aligned} \tag{20}$$

where $\vec{\nabla} \times \vec{\nabla}\rho = 0$. Finally, utilizing $\vec{\nabla}\left(\vec{u} \cdot \vec{u}\right) = \vec{\nabla} \cdot \left(\vec{u} \cdot \vec{u}\mathbf{1}\right)$, Eq.(18) now reads:

$$\begin{aligned}
\kappa \vec{\nabla}\rho \vec{\nabla}^2 \rho &= \kappa \left(\vec{\nabla} \cdot \left(\vec{\nabla}\rho \otimes \vec{\nabla}\rho \right) - \vec{\nabla}\rho \cdot \vec{\nabla}\left(\vec{\nabla}\rho\right) \right) \\
&= \kappa \left(\vec{\nabla} \cdot \left(\vec{\nabla}\rho \otimes \vec{\nabla}\rho \right) \right) \\
- \quad & \kappa \left(\left(\frac{1}{2} \vec{\nabla}\left(\vec{\nabla}\rho \cdot \vec{\nabla}\rho \right) - \vec{\nabla}\rho \times \left(\vec{\nabla} \times \vec{\nabla}\rho \right) \right) \right) \\
&= \kappa \vec{\nabla} \cdot \left(\left(\vec{\nabla}\rho \otimes \vec{\nabla}\rho \right) - \frac{1}{2} \left(\vec{\nabla}\rho \cdot \vec{\nabla}\rho \mathbf{1} \right) \right)
\end{aligned} \tag{21}$$

Thus, capillary-stress tensor for a binary-fluid can be written as [17, 18]:

$$\boldsymbol{\sigma} = \left(p_0 - \frac{1}{2}\kappa \left(\vec{\nabla}\rho \right)^2 \right) \mathbf{1} + \kappa \vec{\nabla}\rho \otimes \vec{\nabla}\rho + \boldsymbol{\sigma}_0 \tag{22}$$

where p_0 is defined in Eq.(13) and $\boldsymbol{\sigma}_0$ represents an arbitrarily constant tensor. Thus, the capillary pressure, p can be obtained as follows:

$$p = \frac{1}{3} \operatorname{tr} \boldsymbol{\sigma} \tag{23}$$

The fluid-fluid interaction strength, w_{ff}, can be calibrated according to the bulk critical temperature, T_c^{3D} [14]:

$$k_B T_c^{3D} = \frac{c w_{ff}}{4} \tag{24}$$

where c denotes the lattice coordination number. The characteristic length scale for lattice can be obtained by combining energy parameter w_{ff} with surface tension, E_s. Estimates for surface energy between liquid-gas interface results in [15]:

$$E_s \sim \frac{w_{ff}}{2a_0^2} \tag{25}$$

The dimensionless form of these parameters read, $\bar{\mu} = \mu/w_{ff}, \bar{T} = k_B T/w_{ff}, \bar{w}_{ff} = w_{ff}/w_{ff}, \bar{w}_{sf} = w_{sf}/w_{ff}$. In what follows, we have utilized a simple cubic lattice in 3D with $c = 6$. From the standard mean field equation of state for lattice with $c = 6$, we expect a critical point located at $\bar{T} = k_B T_c^{3D}/w_{ff} = c/4 = 1.5$ and $\rho_c = 0.5$. The fluid-solid wall interactions can be derived from atomistic simulations (see for e.g. [19]). It is often necessary to calibrate these potentials to reproduce experimental data that depends on fluid-solid interactions such as the isosteric heat of adsorption [20].

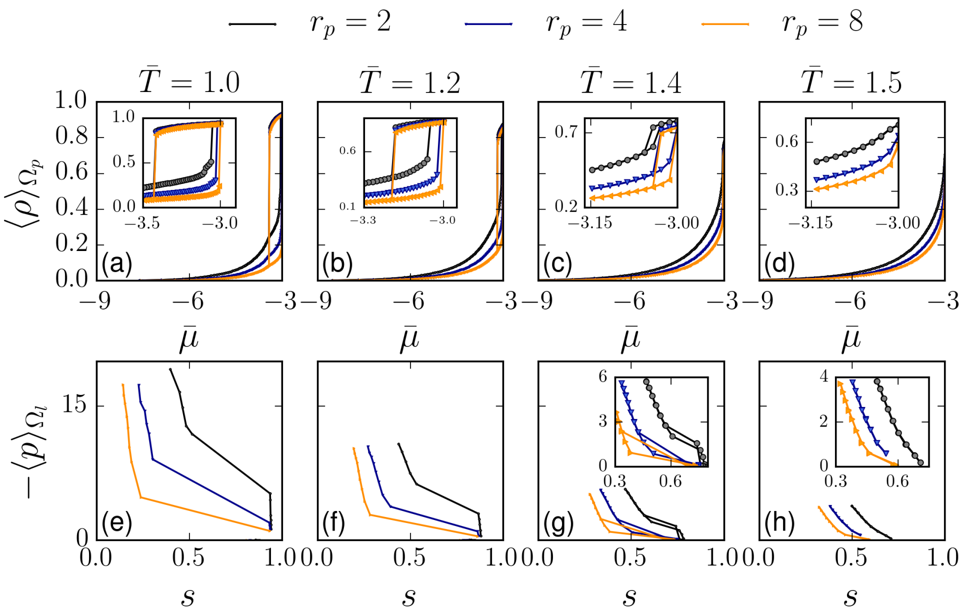

FIG. 3: Isotherms for different cylindrical pores at $\bar{T} = 1.0$ (3a), $\bar{T} = 1.2$ (3b), $\bar{T} = 1.4$ (3c) and $\bar{T} = 1.5$ (3d). Capillary pressure curves for the same pores at $\bar{T} = 1.0$ (3e), $\bar{T} = 1.2$ (3f), $\bar{T} = 1.4$ (3g) and $\bar{T} = 1.5$ (3h).

ISOTHERMS & CAPILLARY CURVES FOR CYLINDRICAL PORES

We performed condensation and evaporation simulations on the same cylindrical pores $L_x = 160$ nm $\ll L_y = L_z$ with pore radius $r_p \in \{2, 4, 8\}$ nm. Reservoirs of length $L_{\text{res.}} = 4$ nm are added to both ends of the cylindrical pore. The capillary condensation and evaporation for these pores are simulated for $a_0 = 0.25$ nm, $y = 2.5$ and $\bar{T} = \{1.0, 1.2, 1.4, 1.5\}$. The isotherms are shown in Figs. 3a-3d and the capillary curves are shown in Figs. 3e-3h.

CRITICAL EXPONENTS FITS

In the vicinity of critical temperature, T_c^{3D}, the following power law singularities for correlation length ξ and connected susceptibility χ are expected [21]:

$$\xi \sim |T - T_c^{3D}|^{-\nu} \tag{26}$$

$$\chi \sim |T - T_c^{3D}|^{\gamma} \tag{27}$$

Given the finite size of the simulation box, L, this divergence cannot be directly observed. However, the simulation data can be extrapolated to $L \to \infty$ using a set of simulation sizes and via finite size scaling analysis. Finite size scaling simply states that at the critical point, $\xi \sim L$, which leads to $\chi_{max} \sim L^{\gamma/\nu}$ and $\mu^* \sim L^{-1/\nu}$. To this end, connected susceptibility $\chi = L^3 \left(\langle \rho^2 \rangle - \langle \rho \rangle^2\right)$ is computed for volumes of characteristic length $L \in \{12, 14, 16\}$ nm for granular media $A - D$ and $\bar{T} = 1.5$ (see Fig. 3 for structure C). These coarse-graining length scales are chosen to be greater than the diameter of the solid particles while providing reasonable statistics (number of realizations, $N > 100$). Additionally, for the porous solid counterparts of granular packings $A - D$, a coarse-graining length scale of $L \in \{7, 8, 9, 10\}$ nm is chosen based on the diameter of the spherical pores. For each realization x, $\chi_{max}\left(x, L\right)$ is obtained. From $\chi_{max}\left(L\right) = \langle \chi_{max}\left(x, L\right) \rangle$ and its corresponding chemical potential $\bar{\mu}^*\left(L\right) = \langle \bar{\mu}^*\left(x, L\right) \rangle$, critical exponents for structures $A - D$ are estimated to be $\nu \in \{0.68, 0.77, 0.88, 0.81\}$ and $\gamma \in \{2.14, 2.43, 2.89, 2.54\}$ for granular packings and $\nu \in \{0.76, 0.82, 0.94, 0.47\}$ and $\gamma \in \{2.21, 2.42, 2.70, 1.39\}$ for their porous solid counterparts. This is achieved by power-law fits of type $y = ax^b$ for $\chi_{max}\left(L\right)$ against L which provides γ/ν and $y = a - x^b$ for $\bar{\mu}^*$ against L^{-1} which leads to ν. These fits are shown in Figs. 4a-4h for granular packings and Figs. 5a-5h for porous solids. The quality of fit measured by R^2 for γ are $0.99, 0.99, 0.99, 0.99$ for granular packings $A - D$ respectively and for γ/ν are $0.62, 0.69, 0.49, 0.70$ for porous solids $A - D$, respectively. Similarly for the porous solids and γ the R^2 values are $0.99, 0.99, 0.99, 0.99$ and for γ/ν are $0.83, 0.71, 0.77, 0.77$ for structures $A - D$, respectively.

SENSITIVITY OF CAPILLARY CURVES TO LOCAL DENSITY THRESHOLD

The liquid domain, Ω_l is determined via a threshold for local density, $\rho\left(\vec{x}_i\right)$. To assess sensitivity of the estimated capillary pressure to the local density threshold, capillary curves for structure C and for $\rho_{\text{th.}} \in [0.5, 0.85]$ are shown in Fig. 6.

HIGHER ORDER CUMULANTS OF CAPILLARY PRESSURE FIELD

Consider the case of a bulk fluid with no confinement - for each imposed increment of chemical potential μ, the PDFs for $\rho\left(\vec{x}\right)$ and $p\left(\vec{x}\right)$ follow a Dirac delta function, i.e.

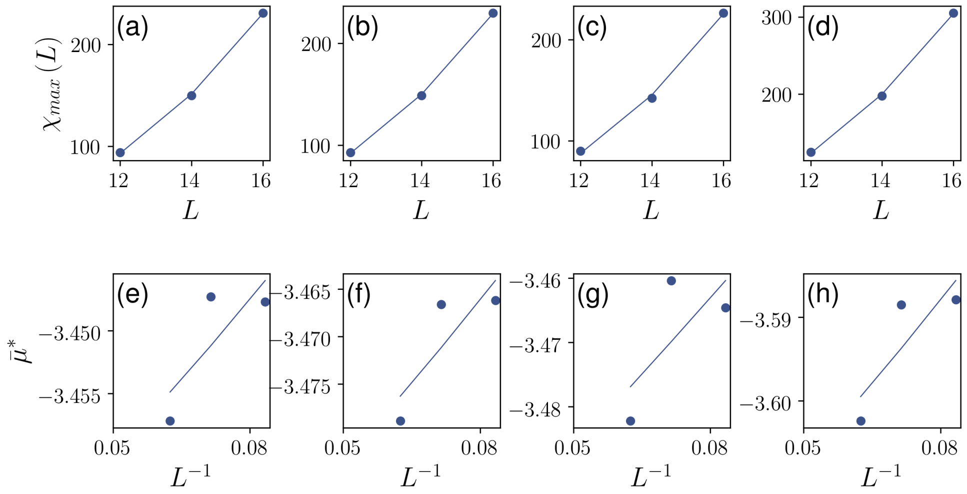

FIG. 4: Power law fit to obtain γ/ν for granular packings $A-D$ (4a-4d) and for ν for granular packings $A-D$ (4e-4h).

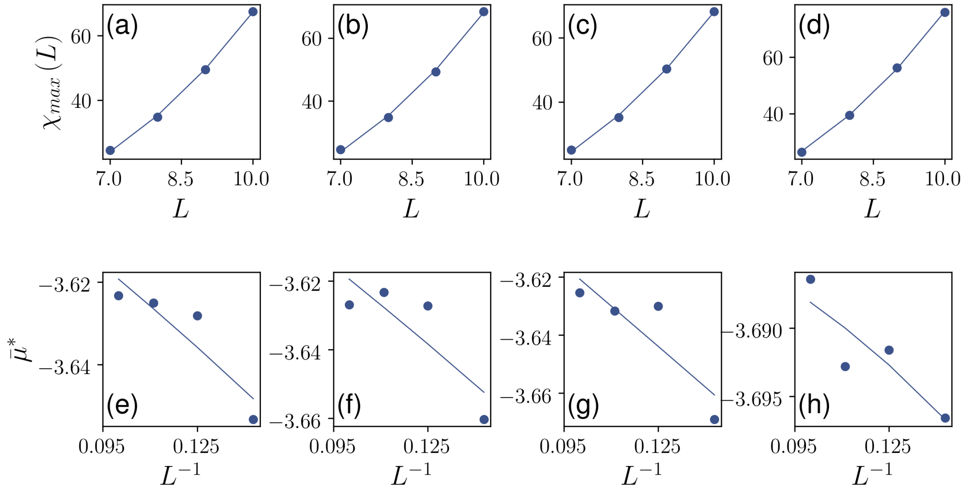

FIG. 5: Power law fit to obtain γ/ν for porous solids $A-D$ (5a-5d) and for ν for porous solids $A-D$ (5e-5h).

no variations in space. This picture changes as soon as the energy landscape is perturbed via introduction of confinement. This effect is explored by simulating a binary fluid inside the described particle packings for $\bar{T} = k_BT/w_{ff} \in \{1.0, 1.2, 1.4, 1.5\}$ and $h = \exp\left(\left(\mu - \mu_{sat}^{3D}\right)/k_BT\right) \in (0, 1]$. For each increment, during both condensation and evaporation, capillary pressure $p(\vec{x})$ scalar field in the pore domain, Ω_p, is characterized using its first four cumulants. In general, given a random variable x, it's mean m_x, variance

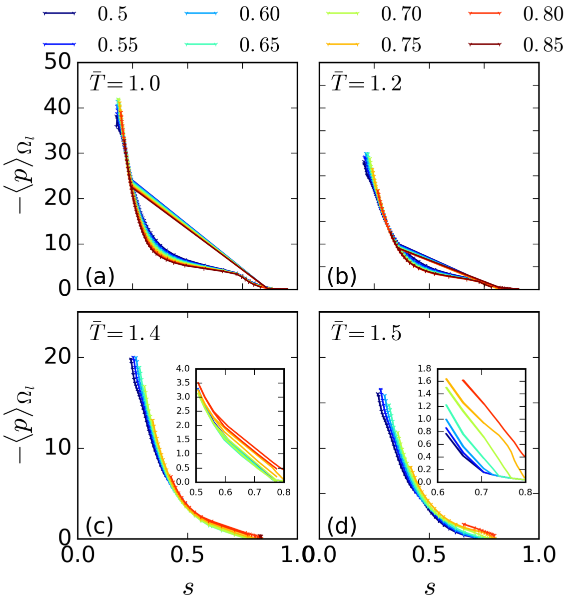

FIG. 6: Sensitivity of capillary pressure estimations to local density threshold for determining liquid domain Ω_l for structure C, $\rho_{\text{th.}} \in [0.5, 0.85]$ and temperatures $\bar{T} = 1.0$ (6a), $\bar{T} = 1.2$ (6b), $\bar{T} = 1.4$ (6c) and $^-$(6d).

v_x, skewness s_x and kurtosis κ_x are defined as:

$$m_x = \langle x\rangle = \frac{1}{n}\sum_i^n x_i \tag{28}$$

$$v_x = \frac{1}{n-1}\sum_i^n (x_i - m_x)^2 \tag{29}$$

$$s_x = \langle (x-m_x)^3\rangle / \langle (x-m_x)^2\rangle^{3/2} \tag{30}$$

$$\kappa_x = \langle (x-m_x)^4\rangle / \langle (x-m_x)^2\rangle^{2} \tag{31}$$

where $p(x)$ is the probability density function of random variable x. Pore domain is defined as all fluid nodes with no solid neighbors. In addition, prior to any analyses, the average pressure of the reservoir $\langle p\rangle_{\Omega_{\text{res}}}$ is subtracted from the capillary pressure scalar field, $p(\vec{x})$. During these simulations, the particle packing remains static. In reality this would imply a high confining pressure compared to capillary stress so that force balance remains satisfied on each particle [22]. The first four cumulants of the capillary pressure field $p(\vec{x})$ in the pore domain Ω_p during both condensation and evaporation are shown in Fig. 7 for mean , Fig. 8 for variance, Fig. 9 for skewness and Fig. 10 for kurtosis.

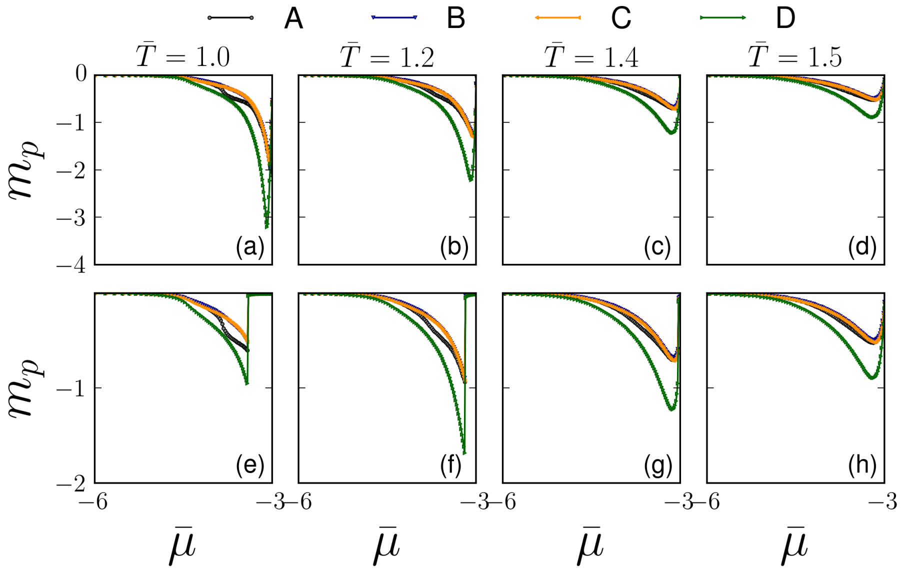

FIG. 7: Evolution of the capillary pressure field in the pore domain, Ω_p characterized by the mean during condensation for $\bar{T} = 1.0$ (7a), $\bar{T} = 1.2$ (7b), $\bar{T} = 1.4$ (7c) and $\bar{T} = 1.5$ (7d) and during evaporation for $\bar{T} = 1.0$ (7e), $\bar{T} = 1.2$ (7f), $\bar{T} = 1.4$ (7g) and $\bar{T} = 1.5$ (7h).

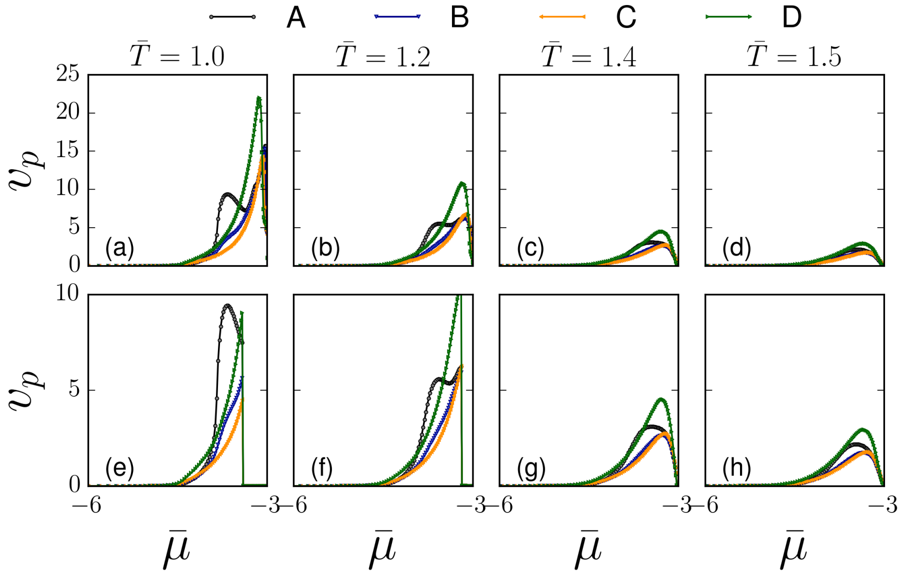

FIG. 8: Evolution of the capillary pressure field in the pore domain, Ω_p characterized by the variance during condensation for $\bar{T} = 1.0$ (8a), $\bar{T} = 1.2$ (8b), $\bar{T} = 1.4$ (8c) and $\bar{T} = 1.5$ (8d) and during evaporation for $\bar{T} = 1.0$ (8e), $\bar{T} = 1.2$ (8f), $\bar{T} = 1.4$ (8g) and $\bar{T} = 1.5$ (8h).

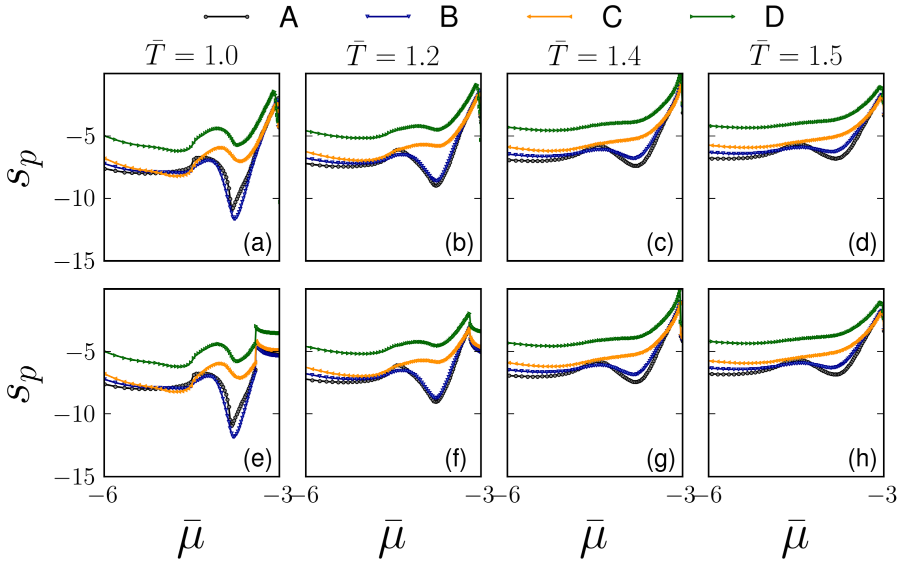

FIG. 9: Evolution of the capillary pressure field in the pore domain, Ω_p characterized by the skewness during condensation for $\bar{T} = 1.0$ (9a), $\bar{T} = 1.2$ (9b), $\bar{T} = 1.4$ (9c) and $\bar{T} = 1.5$ (9d) and during evaporation for $\bar{T} = 1.0$ (9e), $\bar{T} = 1.2$ (9f), $\bar{T} = 1.4$ (9g) and $\bar{T} = 1.5$ (9h).

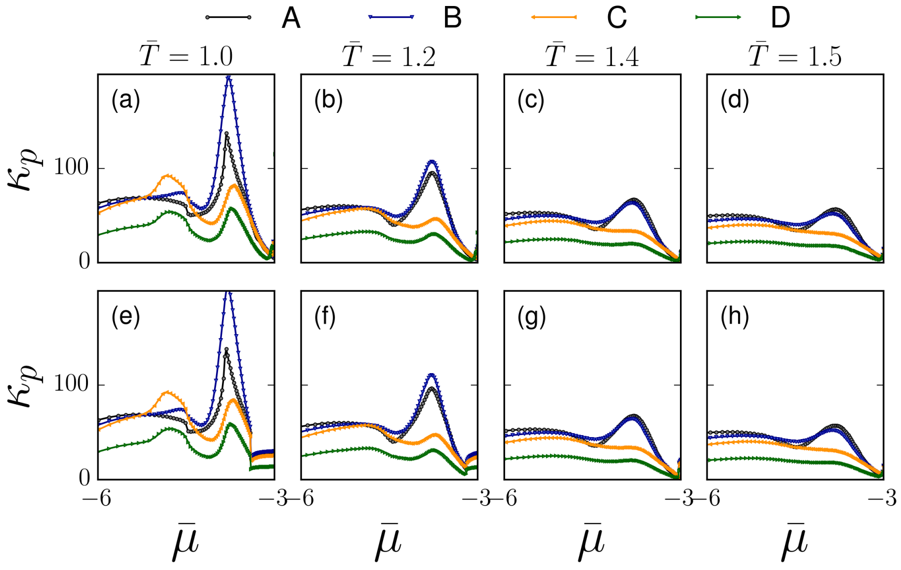

FIG. 10: Evolution of the capillary pressure field in the pore domain, Ω_p characterized by the kurtosis during condensation for $\bar{T} = 1.0$ (10a), $\bar{T} = 1.2$ (10b), $\bar{T} = 1.4$ (10c) and $\bar{T} = 1.5$ (10d) and during evaporation for $\bar{T} = 1.0$ (10e), $\bar{T} = 1.2$ (10f), $\bar{T} = 1.4$ (10g) and $\bar{T} = 1.5$ (10h).

---

[*] monfared@caltech.edu

[†] tingtaoz@caltech.edu

[‡] jandrade@caltech.edu

[§] aikaterini.ioannidou@umontpellier.fr

[¶] franck.radjai@umontpellier.fr

[**] ulm@mit.edu

[††] Roland.pellenq@cnrs.fr

[‡‡] Previously at Department of Civil and Environmental Engineering, Massachusetts Institute of Technology, Cambridge, MA 02139, USA.

[1] S. Torquato, *Random Heterogeneous Materials* (Springer New York, 2002).

[2] H. Laubie, S. Monfared, F. Radjai, R.-M. Pellenq, and F.-J. Ulm, Disorder-induced stiffness degradation of highly disordered porous materials, J. Mech. Phys. Solids **106**, 207 (2017).

[3] H. Laubie, F. Radjai, R. Pellenq, and F.-J. Ulm, Stress transmission and failure in disordered porous media, Physical Review Letters **119**, 10.1103/physrevlett.119.075501 (2017).

[4] S. Plimpton, Fast parallel algorithms for short-range molecular dynamics, J. Comp. Phys. **117**, 1 (1995).

[5] E. Masoero, E. Del Gado, R.-M. Pellenq, F.-J. Ulm, and S. Yip, Nanostructure and nanomechanics of cement: polydisperse colloidal packing, Phys. Rev. Lett. **109** (2012), 3-6.

[6] E. Masoero, E. Del Gado, R.-M. Pellenq, F.-J. Ulm, and S. Yip, Nano-scale mechanics of colloidal c-s-h gels, Soft Matter **10** (2014).

[7] K. Ioannidou, K. Krakowiak, M. Bauchy, C. Hoover, E. Masoero, S. Yip, F.-J. Ulm, P. Levitz, R. Pellenq, and E. Del Gado, Mesoscale texture of cement hydrates, Proc. Natl. Acad. Sci. USA **113**, 2029 (2016).

[8] C. Rycroft, Voro++: A three-dimensional voronoi cell library in c++, Chaos **19** (2009).

[9] L. D. Gelb and K. Gubbins, Pore size distributions in porous glasses: A computer simulation study, Langmuir **15**, 305 (1999).

[10] S. Bhattacharya and K. Gubbins, Fast method for computing pore size distributions of model materials, Langmuir **22**, 7726 (2006).

[11] L. Rayleigh, XX. on the theory of surface forces.—II. Compressible fluids, The London, Edinburgh, and Dublin Philosophical Magazine and Journal of Science **33**, 209 (1892).

[12] J. W. Gibbs, J. Tyndall, and and, *On the equilibrium of heterogeneous substances : first [-second] part* (Published by the Academy, 1874).

[13] E. Kierlik, P. A. Monson, M. L. Rosinberg, L. Sarkisov, and G. Tarjus, Capillary condensation in disordered porous materials: Hysteresis versus equilibrium behavior, Physical Review Letters **87**, 10.1103/physrevlett.87.055701 (2001).

[14] E. Kierlik, P. A. Monson, M. L. Rosinberg, and G. Tarjus, Adsorption hysteresis and capillary condensation in disordered porous solids: a density functional study, Journal of Physics: Condensed Matter **14**, 9295 (2002).

[15] T. Zhou, K. Ioannidou, E. Masoero, M. Mirzadeh, R. J.-M. Pellenq, and M. Z. Bazant, Capillary stress and structural relaxation in moist granular materials, Langmuir **35**, 4397 (2019).

[16] J. W. Cahn and J. E. Hilliard, Free energy of a nonuniform system. i. interfacial free energy, The Journal of Chemical Physics **28**, 258 (1958).

[17] D. Korteweg, Sur la forme que prennent les équations du mouvements des fluides si l on tient compte des forces capillaires causés par des variations de densité con- sidérables mais connues et sur la théorie de la capillarité dans l hypothése d une variation continue de la densité, Archives Néerlandaises des Sciences exactes et naturelles **6**, 1 (1901).

[18] D. Anderson and G. McFadden, *Diffuse-Interface Methods in Fluid Mechanics*, Tech. Rep. NISTIR 6018 (U.S. Department of Commerce, Gathersburg, MD, 1997).

[19] P. A. Bonnaud, Q. Ji, B. Coasne, R. J.-M. Pellenq, and K. J. V. Vliet, Thermodynamics of water confined in porous calcium-silicate-hydrates, Langmuir **28**, 11422 (2012).

[20] B. Coasne, A. Galarneau, R. J. M. Pellenq, and F. D. Renzo, Adsorption, intrusion and freezing in porous silica: the view from the nanoscale, Chemical Society Reviews **42**, 4141 (2013).

[21] M. Fisher, The renormalization group in the theory of critical behavior, Rev. Mod. Phys. **46**, 597 (1974).

[22] J.-Y. Delenne, V. Richefeu, and F. Radjai, Liquid clustering and capillary pressure in granular media, J. Fluid Mech. **762** (2015).